CHEMISTRY OF MATERIALS

pubs.acs.org/cm

Article

Structural Tolerance Factor Approach to Defect-Resistant I_2-II-IV-X_4 Semiconductor Design

Jon-Paul Sun, Garrett C. McKeown Wessler, Tianlin Wang, Tong Zhu, Volker Blum, and David B. Mitzi*

Cite This: *Chem. Mater.* 2020, 32, 1636−1649

Read Online

ACCESS | Metrics & More | Article Recommendations | Supporting Information

ABSTRACT: Recent work on quaternary semiconductors $Cu_2BaSn(S,Se)_4$ and $Ag_2BaSnSe_4$ for photovoltaic and thermoelectric applications, respectively, has shown the promise of exploring the broader family of defect-resistant I_2-II-IV-X_4 materials (where I, II, and IV refer to the formal oxidation state of the metal cations and X is a chalcogen anion) with tetrahedrally coordinated I/IV cations and larger II cations (i.e., Sr, Ba, Pb, and Eu) for optoelectronic and energy-related applications. Chemical dissimilarity among the II and I/IV atoms represents an important design motivation because it presents a barrier to antisite formation, which otherwise may act as electronically harmful defects. We herein show how all 31 experimentally reported I_2-II-IV-X_4 examples (with large II cations and tetrahedrally coordinated smaller I/IV cations), which form within five crystal structure types, are structurally linked. Based on these structural similarities, we derive a set of tolerance factors that serve as descriptors for phase stability within this family. Despite common usage in the well-studied perovskite system, Shannon ionic radii are found to be insufficient for predicting metal−chalcogen bond lengths, pointing to the need for experimentally derived correction factors as part of an empirically driven learning approach to structure prediction. We use the tolerance factors as a predictive tool and demonstrate that four new I_2-II-IV-X_4 compounds, Ag_2BaSiS_4, Ag_2PbSiS_4, Cu_2PbGeS_4, and Cu_2SrSiS_4, can be synthesized in correctly predicted phases. One of these compounds, Ag_2PbSiS_4, shows potentially promising optoelectronic properties for photovoltaic applications.

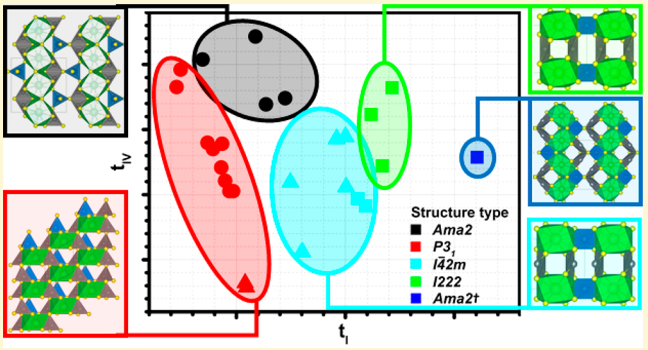

INTRODUCTION

Chalcogenide semiconductors play an important role in a large variety of optoelectronic and energy-related applications, including photovoltaic (PV),[1] thermoelectric (TE),[2] battery,[3−5] transistor,[6,7] photonic,[8] and phase-change memory devices.[9] Among the successful commercial examples are zincblende CdTe and chalcopyrite $Cu(In,Ga)(S,Se)_2$ (CIGSSe), achieving high power conversion efficiency (PCE) in PV devices.[10] The relatively low abundances of elements Te and In, however, present barriers to terawatt deployment of these technologies.[11,12] Kesterite $Cu_2ZnSn(S,Se)_4$ (CZTSSe), in which the In and Ga in CIGSSe are replaced with readily available Zn and Sn, has accordingly received attention as a potential replacement. Yet despite initial progress, the record PCE (12.6%)[13] falls substantially short of that achieved with CIGSSe/CdTe (>20%).[10] This performance shortfall is due in large part to the ionic size and coordination similarity of Cu/Zn/Sn and the associated antisite disorder, which leads to band tailing and deep defects.[14−17] In some classes of solid materials, there is a presumption that as the number of elements exceeds 3−4, entropy dominates, and disorder becomes unavoidable.[18,19] Yet, the ability to tailor a material to a specific application grows with the number of chemical elements available for use in property design, making it desirable to access a larger, not smaller, chemical space for materials synthesis, if the resulting order and phase stability of the material can be controlled. Recently, our group and others have postulated that constituent atom dissimilarity can be used as a design principle to target disorder-*resistant* multinary semiconductors while providing electronic tunability through their multielement nature.[20−23] This principle is demonstrated by $Cu_2BaSnS_{4-x}Se_x$ (CBTSSe), which uses a Ba atom with a larger ionic radius (1.42 Å and 8-fold coordination) in place of the smaller Zn atom of CZTSSe (0.60 Å and 4-fold coordination).[24] CBTSSe has already demonstrated promising performance in PV and photoelectrochemical (PEC) devices, while showing significant reductions in band tailing when compared to CZTSSe.[25−28] When Cu is replaced by Ag, as in $Ag_2BaSnSe_4$ (ABTSe), size and

Received: December 10, 2019
Revised: January 30, 2020
Published: January 30, 2020

https://dx.doi.org/10.1021/acs.chemmater.9b05107
Chem. Mater. 2020, 32, 1636−1649

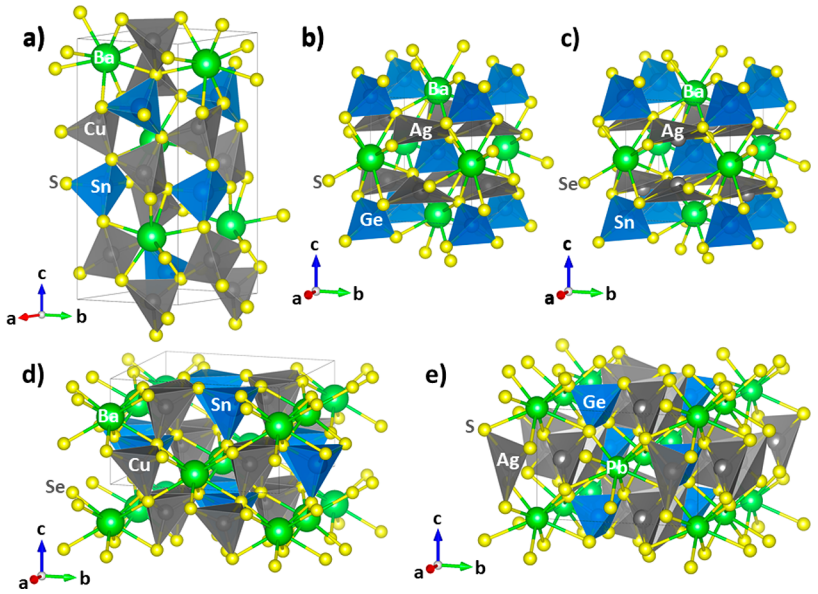

Figure 1. Crystal structures of (a) Cu_2BaSnS_4 (Cu_2SrSnS_4-type, $P3_1$ space group), (b) Ag_2BaGeS_4 ($Ag_2[NH_4]AsS_4$-type, $I\bar{4}2m$ space group), (c) $Ag_2BaSnSe_4$ (Ag_2BaSnS_4-type, $I222$ space group), (d) $Cu_2BaSnSe_4$ ($Cu_2SrGeSe_4$-type, $Ama2$ space group), and (e) Ag_2PbGeS_4 (Ag_2PbGeS_4-type, $Ama2$ space group, later referred to as $Ama2$† to distinguish it from the $Cu_2SrGeSe_4$-type structure). Atom/polyhedra colors are I: gray, II: green, IV: blue, X: yellow.

coordination discrepancy between I and II atoms leads to flattened Ag−Se_4 tetrahedra (Figure 1c), producing low-frequency optical phonon modes through Ag−Ag coupling. Through suppression of acoustic modes, these Ag dimers are predicted to be the origin of the ultralow measured thermal conductivity of ABTSe (0.31 W m^{-1} K^{-1}), making this material an interesting candidate for TE applications.[29,30]

The above examples show that it is worthwhile to explore the broader space of chalcogenide semiconductors defined by combining cations of distinctly different size and coordination. CBTSSe and ABTSe are part of a I_2-II-IV-X_4 (e.g., I = Li, Cu, Ag; II = Ba, Pb, Sr; IV = Si, Ge, Sn; X = S, Se) semiconductor family with 31 experimentally known members (*vide infra*). These materials are composed of similar structural and coordination motifs and are currently under investigation for PV/PEC,[31−33] thermoelectric,[29,34] and nonlinear optical[35,36] applications. However, while size and coordination dissimilarity may act as a design principle to encourage certain types of order, the detailed structures formed will vary sensitively with the chosen composition. This is exemplified by CBTSSe, where the overall structure, and therefore the electronic properties, are determined by the chalcogen ratio, x. As the Se content is increased to $x = 3$, the bandgap narrows and harvests more of the solar spectrum. For larger $x > 3$, the crystal structure changes abruptly from the Cu_2SrSnS_4-type ($P3_1$ space group) to a wider bandgap $Cu_2BaSnSe_4$-type ($Ama2$ space group).[20] The same transition, albeit as a function of Sn (IV) content, can be observed in the related system $Cu_2BaGe_{1-x}Sn_xSe_4$ (CBGTSe) when the Sn content increases above $x = 0.7$.[37] Both CBTSSe and CBGTSe demonstrate that detailed understanding and control of structure are essential to obtain I_2-II-IV-X_4 materials with precisely tailored electronic features. However, despite the clear structure preferences and phase boundaries in experiment, calculated total energy differences between the structure types can be rather subtle (few meV/atom in unit cells with several tens of atoms). As we have found in past work,[31,37] these differences can indeed be too low for current theory—i.e., standard semilocal density functional theory (DFT) and even computationally more costly, relatively advanced hybrid DFT—to properly distinguish different, long-range ordered structures composed of similar building blocks but with different electronic properties. It would therefore be desirable to establish a set of qualitative indicators, i.e., "descriptors", that allow one to predict the structure types of different possible I_2-II-IV-X_4 materials *a priori*, resulting in a much-enhanced ability to infer the likely functional properties of the material, e.g., by follow-up state-of-the-art first-principles calculations.

In this contribution, we propose that an approach based on ionic radii (or more appropriately, bond lengths), akin to the perovskite Goldschmidt tolerance factor,[38] may be used to rationalize current structures and predict new members of the defect-resistant I_2-II-IV-X_4 family. Five distinct crystal structures have been reported for the experimentally known members of the I_2-II-IV-X_4 family, all of which share two key structural features (Figure 1): (1) a three-dimensional (3D) extended network of I/IV metal−chalcogen tetrahedra and (2) a significantly larger II atom adopting nontetrahedral coordination. None of the five structures contain multiple coordination environments for a single atomic species. To demonstrate the usefulness of the tolerance factor hypothesis, we predict the crystal structures of four new compounds— i.e., Ag_2BaSiS_4, Ag_2PbSiS_4, Cu_2PbGeS_4, and Cu_2SrSiS_4[a]—and show that they can be synthesized and characterized in the predicted structure types. We therefore envision that this new tolerance factor approach will facilitate the discovery of a multitude of new defect-controlled semiconducting and energy-related structures (as has been the case for perovskites).

METHODS

Solid State Synthesis. Ag_2S powder (Alfa Aesar 99.995%), Cu_2S powder (Alfa Aesar 99.5%), BaS powder (Materion 99.9%), PbS powder (Sigma-Aldrich 99.9%), SrS powder (Materion 99.9%), Si pieces (Sigma-Aldrich 99.95%), Ge powder (Alfa Aesar 99.999%), SnS powder (Materion 99.5%), and S flakes (Sigma-Aldrich 99.99%) were used as received. Ternary and quaternary compounds were formed by

https://dx.doi.org/10.1021/acs.chemmater.9b05107
Chem. Mater. 2020, 32, 1636−1649

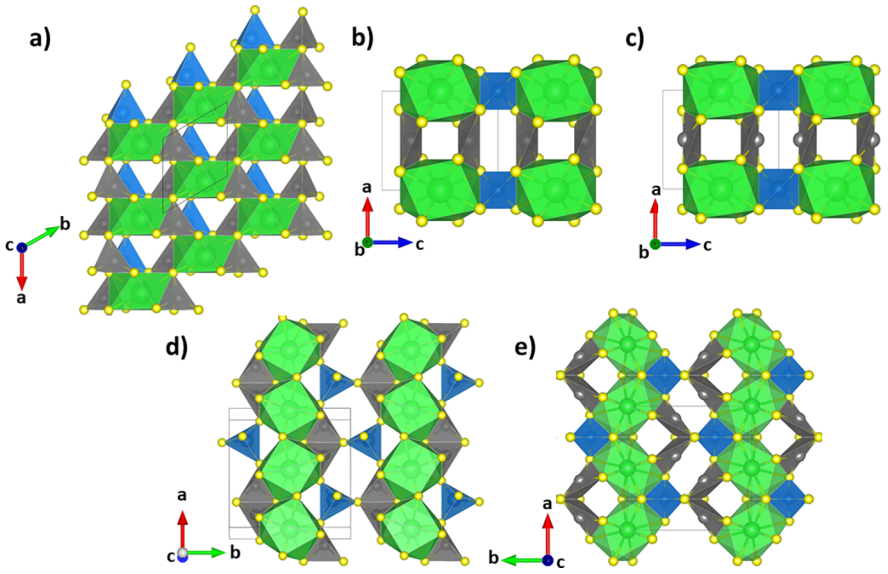

Figure 2. Selected crystallographic views of (a) Cu_2BaSnS_4 ($P3_1$), (b) Ag_2BaGeS_4 ($I\bar{4}2m$), (c) $Ag_2BaSnSe_4$ ($I222$), (d) $Cu_2BaSnSe_4$ ($Ama2$), and (e) Ag_2PbGeS_4 ($Ama2$†) to illustrate connectivity of M−X polyhedra. Atom/polyhedra colors are I: gray, II: green, IV: blue, X: yellow.

combining reagents in stoichiometric amounts with a total mass of ∼250−400 mg. Mixtures were weighed, ground with a mortar and pestle, and cold pressed, all in a N_2-filled glovebox. Ternary I = Ag and quaternary I = Cu compounds were flame-sealed in fused-silica ampules under vacuum (10^{-6} Torr). Quaternary I = Ag compounds were sealed under N_2 to prevent Ag_8SiS_6 from evaporating from the pellets. Ampules were annealed for 96 h at the following temperatures and allowed to cool naturally: Ag_2BaSiS_4 800 °C, Ag_2PbSiS_4 525 °C, Cu_2PbGeS_4 575 °C, Cu_2SrSiS_4 800 °C, and Ag_8SiS_6 800 °C. All compounds were ground, pressed, resealed, and annealed several times to achieve desired phase purity, except for Ag_2BaSiS_4, which only required a single anneal. Cu_2PbSnS_4 synthesis was also attempted at several temperatures between 500 and 1000 °C; however, the only reaction products achieved were Cu_2SnS_3 and PbS.

Characterization. Powder X-ray diffraction (PXRD) patterns were measured using a PANalytical Empyrean diffractometer using Cu Kα radiation under ambient conditions. Diffuse reflectance spectra of powder samples were measured using either an Enlitech QE-R Spectral Response Measurement System (bandgap <3 eV) or a Cary 5000 spectrophotometer equipped with a DRA 2500 diffuse reflectance accessory (bandgap >3 eV). Bandgaps were determined by transforming diffuse reflectance data with the Kubelka−Munk function, $F(R)$, defined as $F(R) = (1 - R)^2/2R$, where R is the diffuse reflectance.[40] Direct [indirect] bandgaps were extracted by determining the onset of absorption from Tauc plots by plotting $(h\nu F(R))^2$ vs $h\nu$ [$(h\nu F(R))^{1/2}$ vs $h\nu$].

Computation. The computational work in this paper employed FHI-aims,[41−45] a high-precision,[46,47] all-electron electronic structure code. FHI-aims relies on numeric atom-centered basis functions for numerical discretization of orbitals and densities. A linear-scaling approach is employed to evaluate hybrid density functionals.[48,49] To assess formation enthalpies and bond lengths of computationally relaxed structures, we used the generalized gradient approximation (GGA) and meta-GGA functionals PBE,[50] PBEsol[51] and SCAN.[52] PBEsol and SCAN are designed to improve lattice constant and enthalpy errors of PBE, respectively.[51,53] We used all three computational approaches to assess the efficacy of the various functionals for predicting stability of the various quaternary chalcogenide systems (relative to experimental results). SCAN calculations were only pursued for Ag_2BaSiS_4 and Cu_2SrSiS_4. For Ag_2PbSiS_4, Cu_2PbGeS_4, and Cu_2PbSnS_4, we did not obtain SCAN results. In these cases, the known[54,55] sensitivity of this functional (as well as other functionals based on the same set of underlying electronic structure descriptors, particularly the so-called iso-orbital indicator) to integration grid density led to spurious difficulties with total energy gradients that prevented a reliable geometry optimization of the relatively complex structures in question. For the computations with both the PBE and PBEsol functional, the default "tight" numerical settings in FHI-aims were employed. For all compounds considered, all unit cell vectors and atomic coordinates were fully relaxed until all total energy gradients with respect to lattice vectors and atomic positions were smaller in magnitude than 10^{-2} eV/Å. For the SCAN functional, more grid points were used to achieve convergence for Ag_2BaSiS_4 and Cu_2SrSiS_4 as well as the secondary compounds competing with their formation.[56] Specifically, we used FHI-aims' "really tight" numerical settings. Furthermore, the radial density of integration grid spheres around each atom was increased by a factor of roughly four, i.e., by adjusting the "radial_multiplier" parameter described in the Appendix of ref 56 from 2 to 8. In the case of the SCAN functional, all residual total energy gradients with respect to lattice vectors and atomic positions were set to be smaller in magnitude than 5×10^{-3} eV/Å. The k-point grids used for the five potential materials, Ag_2BaSiS_4, Ag_2PbSiS_4, Cu_2PbGeS_4, Cu_2PbSnS_4, and Cu_2SrSiS_4, are shown in Table S1 of the Supporting Information. For secondary phases, associated k-point grids appear in Table S2. The optimized unit cell parameters for each primary or secondary compound for each functional considered are also included in Tables S1 and S2.

Band structure calculations for Ag_2BaSiS_4, Ag_2PbSiS_4, Cu_2PbGeS_4, and Cu_2SrSiS_4 were performed using the hybrid exchange-correlation functional HSE06,[57,58] with standard settings for the screening parameter ω (0.2 Å^{-1}) and exchange mixing parameter α (0.25). Their band structures were calculated for experimentally determined quaternary crystal structures using fixed lattice parameters determined from PXRD, relaxing only the atomic coordinates within the cell until the magnitude of the associated total energy gradients was below 5×10^{-3} eV/Å. The Γ-point-centered k-point grids used for HSE06 calculations are listed in Table S3, along with the respective fixed lattice parameters. Brillouin zones and k-space paths are illustrated in Figure S1. Non-selfconsistent spin−orbit coupling (SOC) was included in all band structure computations.[45] Normal-incidence absorption coefficients $\alpha(\omega)$ were calculated at the level of the random phase approximation (RPA) as previously reported.[31] These HSE06 settings have worked well for elements up to 5p/6s orbitals;[31] however, for Pb, we are aware that a much greater SOC error must be expected, especially for the 6p-derived conduction bands.[45] The magnitude of this error is of the same order as the residual error of the bandgap prediction by the exchange functional, but the two are not simply coupled. Different elemental contributions mix in the conduction bands

https://dx.doi.org/10.1021/acs.chemmater.9b05107
Chem. Mater. 2020, 32, 1636−1649

(strongly and weakly affected by relativity), so it is not possible to say *a priori* what the exact uncertainty will be. Refs 45 and 59 estimate the possible magnitude of uncertainty for essentially purely 6p-derived states (the worst case) to be ~0.4 eV.

RESULTS

Formalism. An analysis of the five structure types represented by the I_2-II-IV-X_4 family (Figure 1) begins by examining the geometric relationships between metal−chalcogen polyhedra. For brevity, the structures will henceforth be referred to by their respective space groups, adopting the label *Ama*2† for the Ag_2PbGeS_4-type structure to avoid confusion with the $Cu_2SrGeSe_4$-type *Ama*2 structure (Figure S2 shows a detailed comparison of the *Ama*2 and *Ama*2† structures). In the $P3_1$ structure, there is a 3-fold screw axis along the *c*-direction. Figure 2a shows one layer of the $P3_1$ structure in the *AB*-plane, where the crystal is built up by stacking these layers in the *c*-direction with 120° rotation between each. The II-X_8 (i.e., notation indicates a II atom coordinated by 8 X atoms) dodecahedra (12 sides) are very close to square antiprismatic (10 sides) and share faces with two I-X_4 tetrahedra. Within each layer these [I-X_4][II-X_8][I-X_4] moieties (Figure 3a) stack in a

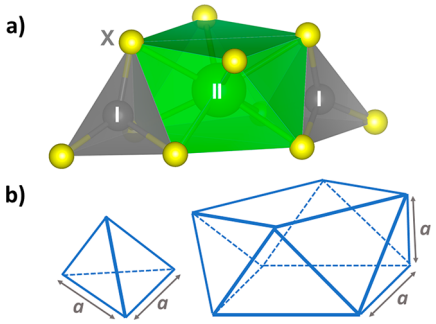

Figure 3. (a) [I-X_4][II-X_8][I-X_4] face-sharing component common to $P3_1$ and *Ama*2 structures (taken from a $Cu_2BaSnSe_4$ unit cell) and (b) dimensions of idealized regular tetrahedron and uniform square antiprism.

brick-like fashion with the IV-X_4 tetrahedra edge sharing with the II-X_8 pseudosquare antiprisms and providing connectivity between adjacent layers. In the *Ama*2 structure (Figure 2d), the same [I-X_4][II-X_8][I-X_4] face-sharing moieties exist; however, they are arranged in a herringbone-type configuration within the *AB*-plane. These layers are then slip stacked in the *c*-direction to build the crystal. Again, the IV-X_4 tetrahedra provide connectivity, this time between herringbone chains. The $I\bar{4}2m$ and *I*222 structures (Figure 2b, c) are nearly identical, namely the former is tetragonal and the latter orthorhombic. They can be distinguished in XRD by symmetry-related splitting of reflection peaks. In these structures the I-X_4 tetrahedra flatten and edge share with the II-X_8 dodecahedra, which have distorted further from square antiprismatic. Finally, the *Ama*2† structure (Figure 2e) forms a similar herringbone-type configuration as the *Ama*2 structure; however, like the $I\bar{4}2m$ and *I*222 structures, the I-X_4 tetrahedra are flattened and edge share with the II-X_8 dodecahedra, which have lost any semblance of the square antiprismatic form observed in the $P3_1$ and *Ama*2 structures.

Unlike the perovskite structure, wherein the simple cubic geometry allows for an exact solution to the stability criterion,[38] the complexity of relating five crystal structures across three lattice systems requires some approximations to construct an analytical tolerance factor expression. Therefore, the outcome of this exercise is not expected to relay rigid stability criteria for a particular structure but rather a qualitative understanding of the phase transitions through the five structures upon atomic substitutions. In the $P3_1$ and *Ama*2 structures, the I-X_4 tetrahedra and II-X_8 polyhedra share faces, constraining their relative sizes. The IV-X_4 tetrahedra share two edges with II-X_8 polyhedra, also constraining their relative sizes. We therefore construct an idealized case where the square antiprisms are assumed uniform and tetrahedra are assumed to be regular, with equal edge length *a* (Figure 3b). Face-sharing between these ideal shapes implies size relationships between the polyhedra. We can then derive two tolerance factors describing the geometric relations as follows (an in-depth tolerance factor derivation is provided in the Supporting Information):

The distance from the center of the tetrahedron to any vertex can be expressed as the sum of the ionic radii of the I (r_I) or IV (r_{IV}) atoms and the X atom (r_X)

$$r_I + r_X = \sqrt{\frac{3}{8}}\,a \tag{1}$$

$$r_{IV} + r_X = \sqrt{\frac{3}{8}}\,a \tag{2}$$

Similarly, the distance from the center of the square antiprism to any vertex can be expressed as the sum of the ionic radii of the II (r_{II}) and X atom

$$r_{II} + r_X = \sqrt{\frac{1}{2} + \frac{1}{4\sqrt{2}}}\,a \tag{3}$$

Finally, eqs 1, 2, and 3 can be combined to define two dimensionless tolerance factors t_I and t_{IV} (where ideally $t_I = t_{IV} = 1$):

$$t_I = \sqrt{\frac{4+\sqrt{2}}{3}}\,\frac{r_I + r_X}{r_{II} + r_X} \tag{4}$$

$$t_{IV} = \sqrt{\frac{4+\sqrt{2}}{3}}\,\frac{r_{IV} + r_X}{r_{II} + r_X} \tag{5}$$

Note that this analysis is more tightly constrained in the $P3_1$ and *Ama*2 structures due to face sharing between I-X_4 and II-X_8 polyhedra, and therefore, t_I values closer to unity are expected. A lower degree of IV-X_4/II-X_8 connectivity in all structures should allow for a larger range of tolerated t_{IV} values, similar to the lower degree of I-X_4/II-X_8 connectivity in the $I\bar{4}2m$, *I*222, and *Ama*2† structures. To date, there are 31 reported large II cation I_2-II-IV-X_4 compounds and 3 studies that examine alloys of end members in different space groups. These compounds are listed in Table 1, with initial tolerance factors derived using Shannon ionic radii[24] plotted in Figure 4a. Note that, for chalcogen atoms, the Shannon ionic radii are only available for 6-fold coordination, whereas for all structures the anions are centered in 5-fold coordination. We use the 6-fold coordination ionic radii without adjustment and assume the small size discrepancy will not significantly affect the results (in later discussion, this issue will be more rigorously addressed by progressing to the use of empirical metal−chalcogen bond lengths within this specific family of compounds).

Based on the tolerance factor plot (Figure 4a), it is apparent that several trends emerge. The majority of I = Cu compounds form in the $P3_1$ space group; however, there exist a few compounds that adopt the *Ama*2 structure in the region where

https://dx.doi.org/10.1021/acs.chemmater.9b05107
Chem. Mater. 2020, 32, 1636−1649

Table 1. Tolerance Factors Calculated Using Shannon Ionic Radii and Average Experimental Bond Lengths Derived from Single Crystal Structures and Structure Types of Reported I_2-II-IV-X_4 Compounds[a]

compound	t_I	t_{IV}	t_I^{exp}	t_{IV}^{exp}	structure type	ref
Ag_2BaGeS_4	1.17	0.92	1.06	0.90	$I\bar{4}2m$	60
$Ag_2BaGeSe_4$	1.18	0.94	1.08	0.93	$I222$	36, 61
$Ag_2BaSiSe_4$	1.18	0.89	1.07	0.90	$I\bar{4}2m$	36
Ag_2BaSnS_4	1.17	0.98	1.07	0.97	$I222$	62
$Ag_2BaSnSe_4$	1.18	1.00	1.08	0.99	$I222$	36, 63
Ag_2PbGeS_4	1.22	0.96	1.15	0.96	$Ama2$†	32, 64
Cu_2BaGeS_4	1.01	0.92	0.99	0.93	$P3_1$	35, 65
$Cu_2BaGeSe_4$	1.02	0.94	0.99	0.95	$P3_1$	33, 37, 61
$Cu_2BaSiSe_4$	1.02	0.89	1.00	0.92	$P3_1$	35
Cu_2BaSnS_4	1.01	0.98	0.98	0.99	$P3_1$	20, 35, 66
$Cu_2BaSnSe_4$	1.02	1.00	0.99	1.01	$Ama2$	20, 35, 37, 63
Cu_2EuGeS_4	1.06	0.97	1.00	0.94	$P3_1$	67, 68
$Cu_2EuGeSe_4$	1.07	0.99	1.03	0.98	$Ama2$	68
Cu_2EuSiS_4	1.06	0.91	1.00	0.91	$P3_1$	68
Cu_2EuSnS_4[b]	1.06	1.04	1.02	1.03	$Ama2$, $P3_1$	67, 69
Cu_2PbSiS_4	1.05	0.90	n/a	n/a	$P3_1$	32, 70
Cu_2SrGeS_4	1.06	0.97	0.99	0.95	$P3_1$	65, 67
$Cu_2SrGeSe_4$	1.07	0.98	1.02	0.98	$Ama2$	61
Cu_2SrSiS_4	1.06	0.91	1.01	0.91	$P3_1$	39
Cu_2SrSnS_4	1.06	1.04	0.98	1.00	$P3_1$	67, 71
Li_2BaGeS_4	1.00	0.92	n/a	n/a	$I\bar{4}2m$	72
$Li_2BaGeSe_4$	1.02	0.94	n/a	n/a	$I\bar{4}2m$	72
Li_2BaSnS_4	1.00	0.98	n/a	n/a	$I\bar{4}2m$	72
$Li_2BaSnSe_4$	1.02	1.00	n/a	n/a	$I\bar{4}2m$	72
Li_2CaGeO_4	1.06	0.95	1.03	0.92	$I\bar{4}2m$	73
Li_2CaSiO_4	1.06	0.88	1.04	0.86	$I\bar{4}2m$	73
Li_2EuGeS_4	1.06	0.97	1.06	0.95	$I\bar{4}2m$	74
Li_2EuSiO_4	1.01	0.84	1.01	0.84	$P3_1$	75
Li_2PbGeS_4	1.04	0.96	1.05	0.95	$I\bar{4}2m$	74
Li_2SrSiO_4	1.01	0.84	1.01	0.84	$P3_1$	75
Li_2SrSiS_4	1.05	0.91	1.06	0.91	$I\bar{4}2m$	39

[a]n/a: data not available. [b]Experimental tolerance factors (based on single crystal structures) are only available for the *Ama*2 structure.

t_{IV} is closer to unity. In the $P3_1$ structure, opposite sides of the IV-X_4 tetrahedra share edges with II-X_8 polyhedra. In contrast, in the *Ama*2 structure, two adjacent sides are edge-sharing, with an additional corner shared (Figure 5). The higher degree of connectivity in the *Ama*2 structure may possibly explain the stricter limitations on the t_{IV} values in compounds that adopt this structure. There exists one compound, Cu_2EuSnS_4, where both $P3_1$[67] and *Ama*2[69] structures have been reported. However, only in the *Ama*2 study do the authors explicitly state that the reaction product was quenched from high temperature, suggesting (reminiscent of our groups' earlier computational results for CBGTSe)[37] that there may be subtle enthalpic differences between these two structures for this chemical composition.

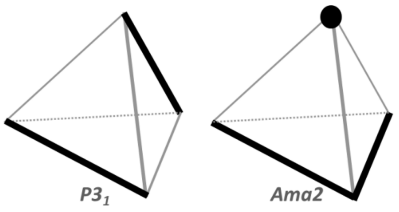

Figure 5. Shared edges and corners of IV-X_4 tetrahedra in $P3_1$ and *Ama*2 structures indicated in black.

The *t* values represent the size ratio of the tetrahedra to the square antiprisms. For I = Ag compounds, the I-X_4 tetrahedra are too large (i.e., $t_I \gg 1$) to face share with the II-X_8 square antiprisms and flatten, edge-sharing as seen in the $I\bar{4}2m$, $I222$, and *Ama*2† structures. In the alloyed system $Cu_{2-x}Ag_xBaSnS_4$, pure phase $P3_1$ is present for $1.01 \leq t_I \leq 1.07$ ($0 \leq x \leq 0.8$). For $1.07 < t_I < 1.13$ ($0.8 < x < 1.5$) there exists a mixed-phase region, with pure phase $I222$ present for larger t_I or *x* values.[66] Because the tolerance factors are derived using the local geometry of $P3_1$ and *Ama*2 structures, in the I = Ag region of the tolerance plot (Figure 4a), it is expected that the model becomes less precise, and structural differences between $I\bar{4}2m$, $I222$, and *Ama*2† structures might not be fully captured. There does appear to be some clustering of phase stable regions for I = Ag compounds; however, with the limited number of data points, this aspect remains inconclusive.

I = Li compounds appear somewhat anomalous when compared to I = Cu, given that Li^+ (0.59 Å) and Cu^+ (0.60 Å) are claimed to have nearly identical ionic radii in Shannon's compilation.[24] There are compositionally analogous Li/Cu pairs that overlap in tolerance factor yet form distinct $I\bar{4}2m/P3_1$

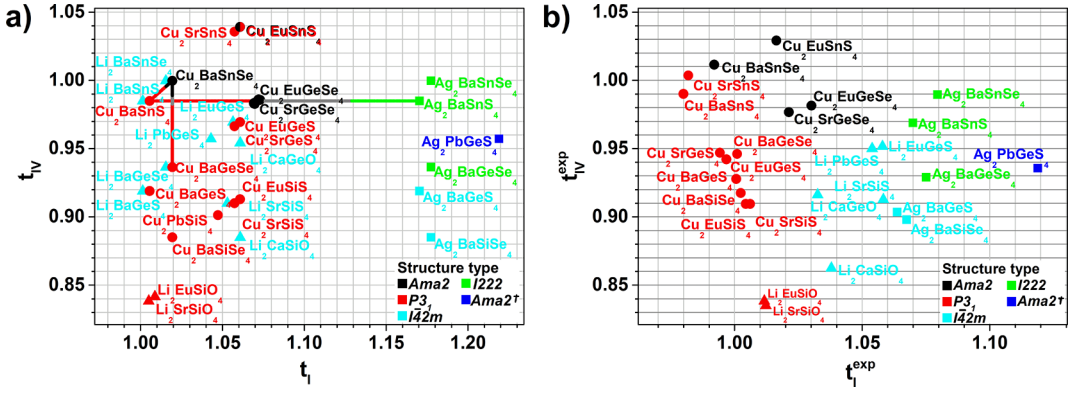

Figure 4. Tolerance factors of reported I_2-II-IV-X_4 compounds calculated using (a) Shannon ionic radii and (b) experimental bond lengths derived from single crystal structures (I = Ag: squares; Cu: circles; Li: triangles). Colors represent different structure types, as noted in the legend. Lines connecting data points show phase progression for alloys with gray line segments representing mixed-phase regions. Cu_2EuSnS_4 has been reported in both $P3_1$ and *Ama*2 space groups.

https://dx.doi.org/10.1021/acs.chemmater.9b05107
Chem. Mater. 2020, 32, 1636−1649

structures. Larger bond lengths in Li vs Cu compounds have been previously observed and are rationalized by the larger ionic character of Li−X bonds, where larger anion electron density leads to increased anion−anion repulsion.[76] If we examine a particular pair where single crystal X-ray analysis has been performed for both compounds Cu_2EuGeS_4[68] and Li_2EuGeS_4,[74] we find Cu−S average bond lengths of 2.34 vs 2.46 Å for Li−S bonds, while the Eu−S average bond lengths remain similar (3.11 vs 3.12 Å). This represents an approximate 5% increase in the effective t_I values for I = Li compounds, lifting the apparent overlap of $P3_1$ and $I\bar{4}2m$ phase regions. This concept is illustrated in Figure 4b, where the experimental tolerance factors (t_I^{exp}, t_{IV}^{exp})—i.e., tolerance factors derived directly from experimentally obtained interatomic distances instead of from Shannon radii—for 26 I_2-II-IV-X_4 compounds are plotted (experimental tolerance factors are also listed in Table 1). For the experimental values, eqs 4 and 5 have been modified such that $r_M + r_X$ is replaced with $\overline{R_{M-X}}$, where $\overline{R_{M-X}}$ is the average metal (M)−chalcogen (X) bond length per metal species in each compound, derived from the single crystal structures.

The stark contrast in clearly identifiable phase regions when using experimental bond lengths (Figure 4b) compared to Shannon radii (Figure 4a) implies that the tolerance factor approach should ultimately provide a valuable predictive tool for assessing other unknown members of this family; however, correction factors are required if using Shannon radii and the original eqs 4 and 5. As a starting point, we propose to "learn" the corrections using additional data from the Inorganic Crystal Structure Database (ICSD) for all reported I_2-II-IV-X_4 materials (i.e., including smaller II atoms such as Cd or Zn), where (1) I = Ag, Cu, or Li; (2) the structures were determined from room-temperature single crystals; and (3) there is a single atomic species per lattice site (no site disorder). Figure 6 shows the ratio

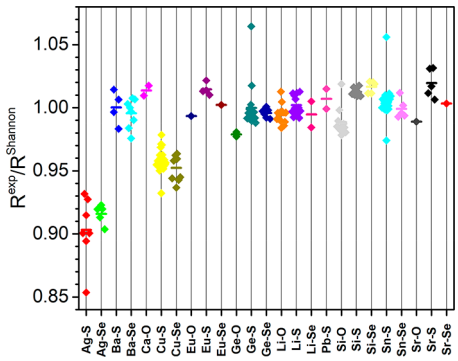

Figure 6. Ratio of experimental bond length to predicted bond length using Shannon ionic radii.[24] Small horizontal lines indicate averages.

of experimental bond lengths to predicted bond lengths using Shannon ionic radii (small-radii II atoms have been omitted from this plot). There are a few M−X bond types where the data have larger variance (e.g., Ag−S and Cu−S), although most are within ∼2% of the average values. Figure S4 shows that similar ratios are achieved when comparing experimental bond lengths to those predicted by Shannon *crystal* radii. These data-driven ratios can directly be used as correction factors because they are readily available and are representative of the class of materials under study. Furthermore, these values can be used for predicting future compounds and are expected to improve as more data become available.

In metal-halide perovskites, attempts have been made to correct bond lengths derived from Shannon radii using electronegativity differences. Indeed, positive correlations between the difference in actual vs expected bond lengths and electronegativity differences have been found.[77] If we consider electronegativity differences in, for example, sulfide bonds for Ag, Cu, Li, Si, Ge, and Sn (Table 2), we can see that, for this class

Table 2. Pauling[78] ($\Delta\chi_P$), Mulliken[79] ($\Delta\chi_M$), and Allred−Rochow[80] ($\Delta\chi_{AR}$) Electronegativity Difference with Sulfur for Select Elements and the Ratio of Average Sulfide Bond Length (R_{M-S}^{avg}) to Shannon Predicted Bond Length ($R_{M-S}^{Shannon}$)[24]

element	$\Delta\chi_P$	$\Delta\chi_M$ (eV)	$\Delta\chi_{AR}$	$R_{M-S}^{avg}/R_{M-S}^{Shannon}$
Ag	0.65	4.60	1.02	0.903
Cu	0.68	4.56	0.69	0.957
Li	1.60	6.03	1.47	1.001
Si	0.68	1.74	0.70	1.013
Ge	0.57	1.51	0.42	1.000
Sn	0.62	1.99	0.72	1.005

of materials, there are no trends with the ratios of experimental bond lengths to Shannon predicted bond lengths. Thus, attempting to correct for electronegativity differences while using Shannon radii in these multinary chalcogenide materials would likely be an unproductive pathway.

Although tolerance factors have been instrumental in the exploration of perovskite compounds, additional structural considerations have recently been applied. The octahedral factor has been introduced to account for the ratio of metal to ligand radii to predict the most stable coordination.[77,81] In the I_2-II-IV-X_4 system, r_{II}/r_X should be 0.732−1.000 for dodecahedral coordination and $r_{I,IV}/r_X$ = 0.225−0.414 for tetrahedral. A similar analysis could be applied to determine if, for example, Te could be incorporated into these structures. However, as pointed out by Cahen in a study of the bonded radii in ternary chalcopyrites, the concept of a spherical atom approximation in asymmetric coordination environments (i.e., chalcogen atoms bonded to multiple atomic species) should be abandoned.[82] For chalcogenide compounds, the use of bond lengths (especially from known structures), rather than ionic radii, therefore has a sounder fundamental basis.

Structure Prediction. Lately there has been a trend in materials exploration to move toward machine learning for predicting new compounds. Machine learning algorithms have been successfully applied to binary compounds to predict crystallization in zinc blende, wurtzite, or rock salt structures, using a training data set of 82 known compounds.[83−85] A more ambitious study found a descriptor for 64 prototypical binary crystal structures using a training set of 2105 compounds.[86] A descriptor for ternary metal alloys of the form AB_2C to determine whether they will form the Heusler structure has also been resolved using a training set of 1948 compounds.[87] Yet as the number of elements in the descriptor increases, the so-called "curse of dimensionality" necessitates an exponentially larger data set.[88] For the quaternary materials analyzed in this study, a traditional brute force descriptor is unlikely to be found based on only 31 known compounds. Interestingly, our study raises the possibility that just predicting (or "learning") the bond lengths, which is a much simpler operation, could yield a reliable descriptor when coupled to the tolerance factor approach. Thus, from the data aggregated in Figure 6, we now produce a

https://dx.doi.org/10.1021/acs.chemmater.9b05107
Chem. Mater. 2020, 32, 1636−1649

predictive plot using tolerance factors that have been calculated using average experimental bond lengths (t_I^{avg}, t_{IV}^{avg}). Here, eqs 4 and 5 have been modified to substitute $r_M + r_X$ with the global average r_{M-X} bond length from the ICSD data. We map out five potential new (previously unknown) I_2-II-IV-X_4 compounds in different regions of the phase diagram: Ag_2BaSiS_4, Ag_2PbSiS_4, Cu_2PbGeS_4, Cu_2PbSnS_4, and Cu_2SrSiS_4, as shown in Figure 7. These candidates will be the focus of the experimental work in this study.

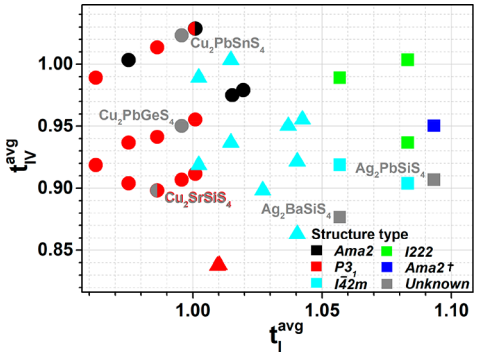

Figure 7. Tolerance factors of reported and potential I_2-II-IV-X_4 compounds that have been corrected using average experimental bond lengths (I = Ag: squares; Cu: circles; Li: triangles), using the same data for average experimental bond lengths as for Figure 6. The compounds included in the figure are the same as those for Figure 4; however, compound labeling has been left off to facilitate identifying the proposed new members of the I_2-II-IV-X_4 family. Compound labels can be found in Figure S5. Cu_2SrSiS_4 was independently reported in the $P3_1$ structure during the review process for this manuscript.[39]

The segregation of distinct structure types into well-separated regions of the tolerance factor plot for Figure 7 (using average experimental bond lengths) is not as perfect as for Figure 4b (using the bond lengths determined for each individual structure), especially for *Ama*2. Yet, there remain regions of clear phase homogeneity and definition of these boundaries is expected to improve as additional related structures are determined and included in the data used to predict average bond lengths. Tolerance factors of the five hypothetical compounds: Ag_2BaSiS_4, Ag_2PbSiS_4, Cu_2PbGeS_4, Cu_2PbSnS_4, and Cu_2SrSiS_4 are listed in Table 3, along with the most likely

Table 3. Tolerance Factors and Nearest Phase Regions of Hypothetical Compounds Investigated in This Study

compound	t_I^{avg}	t_{IV}^{avg}	phase region
Ag_2BaSiS_4	1.06	0.88	$I\bar{4}2m$
Ag_2PbSiS_4	1.09	0.91	$I\bar{4}2m$/*I*222/*Ama*2†
Cu_2PbGeS_4	1.00	0.95	$P3_1$
Cu_2PbSnS_4	1.00	1.02	*Ama*2/$P3_1$
Cu_2SrSiS_4	0.99	0.90	$P3_1$

stable phase(s) as predicted from Figure 7. Ag_2BaSiS_4 is predicted to form the $I\bar{4}2m$ structure, similar to the analogous selenide compound $Ag_2BaSiSe_4$.[36] Ag_2PbSiS_4 is located in a region of the plot where the data point density is too low to predict the most stable phase, with $I\bar{4}2m$, *I*222 and *Ama*2† all forming phase regions in close proximity. The closest known compound in composition, Ag_2PbGeS_4, has been reported in the *Ama*2† phase.[32,64] Both Cu_2PbGeS_4 and Cu_2SrSiS_4 are clearly in regions where only $P3_1$ compounds have been shown to form. Cu_2PbSnS_4 is located near both $P3_1$ and *Ama*2 compounds, with the nearest data point being Cu_2EuSnS_4 which has been reported in both structures.[67,69]

Synthesis. Using solid state syntheses, four of the five compounds have been found to form quaternary materials. Cu_2PbSnS_4 was attempted at several temperatures between 500 and 1000 °C, but the reaction consistently yielded Cu_2SnS_3 and PbS. The inability to form Cu_2PbSnS_4 highlights one deficiency of the geometric tolerance factor model—i.e., it cannot predict stability of the quaternary phases relative to competing binary and ternary phases. PXRD spectra of the four quaternary compounds are shown in Figure 8 along with the predicted patterns from the HSE06 computationally relaxed structures (*vide infra*). Ag_2BaSiS_4 forms a pale yellow material in the $I\bar{4}2m$ structure, consistent with the predictions based on the tolerance factors. Ag_2PbSiS_4 forms a dark-red material in the *Ama*2† structure, similar to the Ge-containing related material Ag_2PbGeS_4.[32,64] It is interesting to note that this material adopts an orthorhombic space group with a nominally tetragonal unit cell (i.e., $a = b$). The PXRD pattern for this compound indicates apparent preferential orientations, with significant differences in peak intensities compared to the calculated pattern and a near absence of the 231 and 322 diffraction peaks. We have modeled this preferential orientation using five sets of planes and are able to qualitatively capture the observed differences in peak intensities (Figure S6). Over a wide range of synthesis temperatures, Ag_8SiS_6 appears as a consistent impurity phase. Using XRD peak intensities, the estimated amount of secondary impurity phase is approximately 10%. Given the difficulty in removing Ag_8SiS_6, this suggests the energetic difference between the quaternary compound and a phase mixture involving the impurity is small. Cu_2PbGeS_4 and Cu_2SrSiS_4 form gray and grayish-yellow materials, respectively, both in the $P3_1$ structure. It is expected that the color in Cu_2SrSiS_4 originates from $Cu_{2-x}S$ impurities (approximately 2%) due to the calculated wide bandgap (*vide infra*). Cu_2PbGeS_4 contains several unidentified trace (almost below the detection limit) impurity peaks that could possibly be oxide phases. Single-phase Pawley fits of the experimental PXRD patterns to simulated patterns were used to determine experimental lattice parameters (Table 4).

Comparison to Stability Assessment by Current Density Functional Approximations. As shown above (Figure 4b in particular), the tolerance factor approach proposed here, and applied with adequate geometric input data, can predict with remarkable clarity *which* particular structure of a quaternary sulfide or selenide might form, assuming that such a quaternary compound is stable at all. Alternatively, the current *de facto* standard approach to predict which structure out of different possibilities will form is DFT, based on various established but approximate exchange-correlation functionals. It is therefore of interest to compare straightforward DFT calculations to the tolerance factor approach. Based on the experimental findings above, this comparison can help shed light on two interesting questions: (1) How well are typical, straightforward DFT calculations able to discriminate between the different quaternary structures considered for a given compound, compared to the tolerance factor approach? (2) How capable are different density functional approximations of determining whether a given quaternary compound will form at all or whether some alternative equilibrium of unary, binary and/or ternary phases will be more stable than the anticipated quaternary phase? For

https://dx.doi.org/10.1021/acs.chemmater.9b05107
Chem. Mater. 2020, 32, 1636−1649

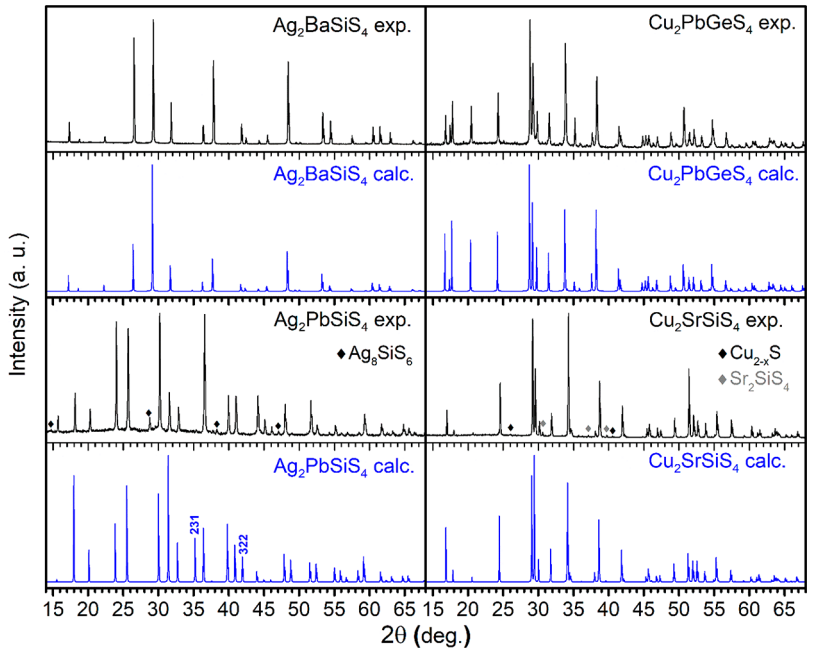

Figure 8. Experimental and calculated PXRD spectra of Ag_2BaSiS_4, Ag_2PbSiS_4, Cu_2PbGeS_4, and Cu_2SrSiS_4. Impurity peaks indicated by diamond symbols are identified from Joint Committee on Powder Diffractions Standards (JCPDS) reference patterns: Ag_8SiS_6 01-071-0182; $Cu_{2-x}S$ 01-088-2158; Sr_2SiS_4 00-024-1234.

Table 4. Experimental Lattice Parameters and Bandgaps

		PXRD fit parameters					band gap (eV)		
compound	structure type	*a* (Å)	*b* (Å)	*c* (Å)	vol (Å^3)	GOF	HSE06[a]	Tauc direct	Tauc indirect
Ag_2BaSiS_4	$I\bar{4}2m$	6.75053(2)	6.75053(2)	7.99643(3)	364.396(3)	2.24	1.96 (I)	2.70(5)	2.2(2)
Ag_2PbSiS_4	*Ama*2†	9.8698(7)	9.8697(5)	6.9791(2)	679.9(1)	1.49	2.13 (D)	2.0(1)	1.9(1)
Cu_2PbGeS_4	$P3_1$	6.1252(1)	6.1252(1)	15.3332(2)	498.20(2)	1.60	1.47 (I)	1.78(5)	1.55(5)
Cu_2SrSiS_4	$P3_1$	6.06874(6)	6.06874(6)	15.1373(1)	482.81(1)	1.58	3.30 (I)	3.4(3)	3.4(3)

[a](I): Indirect, (D): Direct.

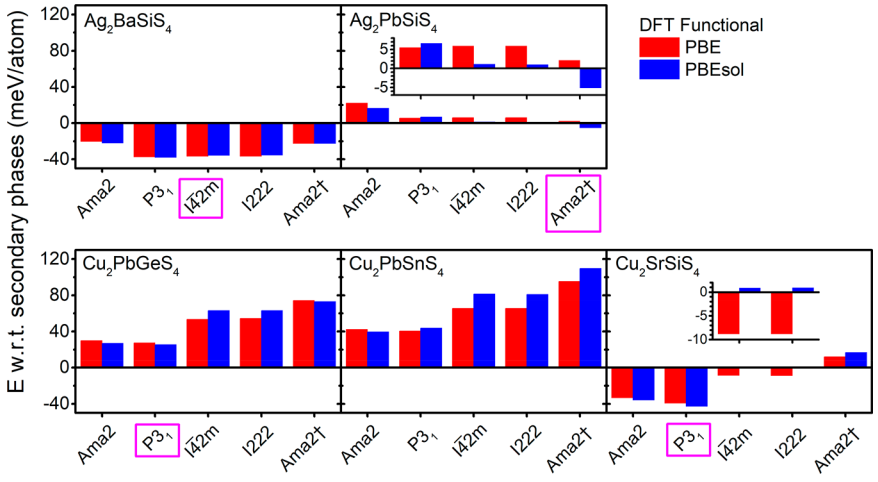

Figure 9. DFT calculated formation energies of the considered quaternary compounds with respect to secondary phases (as defined in eqs 6−10). Positive energies indicate that the phase is unstable. Magenta boxes show experimentally determined quaternary phases (no stable quaternary phase was obtained for Cu_2PbSnS_4). Insets expand the *y*-axis for data points directly underneath.

example, as shown above, Cu_2PbSnS_4 would be expected to form in the *Ama*2 or $P3_1$ structures, or both, if it did form as a quaternary compound; however, experimentally, the quaternary phases appear to be disfavored compared to a competing mix of binary and ternary compounds. Predicting stability over competing phase mixture equilibria is a question that, as yet, eludes the tolerance factor approach, but it is not clear how well typical density functional approximations would perform.

To gain some insights into these questions, we consider three different commonly used semilocal DFT functionals, namely

https://dx.doi.org/10.1021/acs.chemmater.9b05107
Chem. Mater. 2020, 32, 1636−1649

PBE,[50] PBEsol,[51] and (for two compounds only, due to the numerical issues indicated in the Methods section) SCAN.[52] PBE is a generalized gradient approximation (GGA) to the exchange-correlation energy and is frequently used for assessing formation enthalpies. A variant of this functional, PBEsol, improves upon the lattice constant predictions in solids but comes at the cost of reduced accuracy in formation energies.[51] SCAN, a meta-GGA, includes the electronic kinetic energy density and has been shown to reduce errors in formation energies while improving crystal structure selection in binary solids, compared to PBE.[53] For the computational analysis, the atomic positions and lattice parameters of each target quaternary compound listed in Table 3 were fully relaxed in all five crystal structures for each of the three functionals considered. We assess quaternary compound stabilities against secondary phases observed during experimental optimization of syntheses according to the following balanced decomposition reactions:

$$Ag_2BaSiS_4 \rightarrow \frac{1}{4}Ag_8SiS_6 + \frac{1}{2}Ba_2SiS_4 + \frac{1}{4}SiS_2 \quad (6)$$

$$Ag_2PbSiS_4 \rightarrow \frac{1}{4}Ag_8SiS_6 + \frac{1}{2}Pb_2SiS_4 + \frac{1}{4}SiS_2 \quad (7)$$

$$Cu_2PbGeS_4 \rightarrow Cu_2GeS_3 + PbS \quad (8)$$

$$Cu_2PbSnS_4 \rightarrow Cu_2SnS_3 + PbS \quad (9)$$

$$Cu_2SrSiS_4 \rightarrow \frac{1}{2}Cu_2SiS_3 + \frac{1}{2}Cu_2S + \frac{1}{2}Sr_2SiS_4 \quad (10)$$

Figure 9 shows the formation energies for each of the five phases with respect to the secondary phases identified in the decomposition reactions. SCAN data for Ag_2BaSiS_4 and Cu_2SrSiS_4 are given in Figure S7. In line with our previous experiences,[31,37] the formation energy differences between certain adjacent phases within the tolerance plot (e.g., *Ama*2 vs $P3_1$, $I\bar{4}2m$ vs $I222$) are less than 5 meV/atom. Such small enthalpy differences have been observed in polymorphs of TiO_2 and FeS_2[89,90] with first-principles investigations revealing that GGA/meta-GGA (e.g., PBE, PBEsol, SCAN) and hybrid (e.g., HSE06) functionals are of limited reliability in predicting subtle phase competitions, and more expensive higher-level methods are needed to quantify total energies.[91,92]

Regarding previously mentioned question (1), the relative stability of the different quaternary phases with respect to one another is largely but not fully captured for all considered compounds and functionals. For three compounds (Cu_2SrSiS_4, Cu_2PbGeS_4, and Ag_2PbSiS_4), the lowest-energy quaternary phase for the different functionals is the one that forms experimentally, although by strikingly tiny margins (few meV/atom). For Ag_2BaSiS_4, PBE and PBEsol do not predict the experimental phase $I\bar{4}2m$ correctly (again, by a very small margin), while the newer SCAN functional reproduces the experimentally observed result. Given that electronic properties can vary significantly with the underlying structure even if the total-energy difference is small,[31,37] the tolerance factor approach here offers useful additional information that can constrain the space of compounds suspected of forming a given quaternary structure.

Regarding question (2), Figure 9 shows that the different density functionals considered are not fully successful at unambiguously predicting stability over secondary phases. For Ag_2BaSiS_4 and Cu_2SrSiS_4, all functionals considered predict overall stability of the quaternary compounds, in line with the experimental findings. Ag_2PbSiS_4, on the other hand, is predicted to be on the verge of stability, within a few meV/atom margin, similar to some of the subtle energy differences seen between different quaternary structures. The marginal stability is consistent with the experimentally observed difficulty in achieving a phase pure sample—i.e., secondary phases are observed in accordance with equation 7. For Cu_2PbSnS_4 (which could not be formed in experiment), the secondary phases are predicted to be more stable than any of the five considered quaternary structure types, with the closest being ~40 meV/atom higher in energy (*Ama*2, $P3_1$). Among the five compounds examined, Cu_2PbSnS_4 shows the largest positive energy values for the quaternary phases relative to the ternary/binary secondary phases, and therefore, it is reasonable that this system should not form one of the predicted quaternary structures. For Cu_2PbGeS_4, however, which can be made experimentally, the computational results are qualitatively similar to those of Cu_2PbSnS_4, in that the experimentally realized phase ($P3_1$) is predicted to fall 25 meV/atom higher in energy than the decomposition products—i.e., the computational expectation based on DFT-PBE and DFT-PBEsol total energy differences contradicts the experimental observation. Taking Cu_2PbGeS_4 as a rough baseline for the error in the semilocal DFT formation energies, a reasonable tentative conclusion might be that attempting to form a quaternary species over a wide range of reaction conditions might be considered a reasonable pursuit if *any* of the five quaternary phases are predicted to be <30 meV/atom higher in energy than secondary phases. Additional improvements of the DFT energy differences are expected to arise from considering finite-temperature vibrational and lattice expansion contributions to the respective free energies, but these are computationally and technically more involved. Because the current objective was to assess simple strategies to obtain promising predictions, vibrational free energy contributions were not pursued above.

Finally, another possible use of DFT predictions is to use relaxed bond lengths from computational methods to improve the accuracy of the predicted tolerance factors in cases where reliable *a priori* geometry information is not available. In Figure 10, we compare the ratio of the bond lengths predicted by each functional to the average experimental bond lengths (determined from ICSD I_2-II-IV-X_4 crystal structures, Figure 6). As expected, PBE tends to overestimate the bond lengths while PBEsol and SCAN tend closer to ratios of 1.[51] However, due to the functional form of the tolerance factor, systematic errors in bond lengths are subject to cancellation when calculating *t*

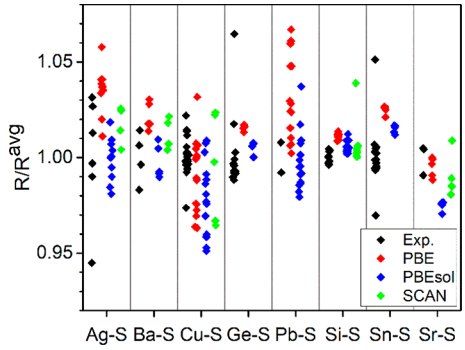

Figure 10. Ratio of DFT predicted bond lengths to the average experimental bond lengths from similar I_2-II-IV-X_4 chalcogenide materials.

https://dx.doi.org/10.1021/acs.chemmater.9b05107
Chem. Mater. 2020, 32, 1636−1649

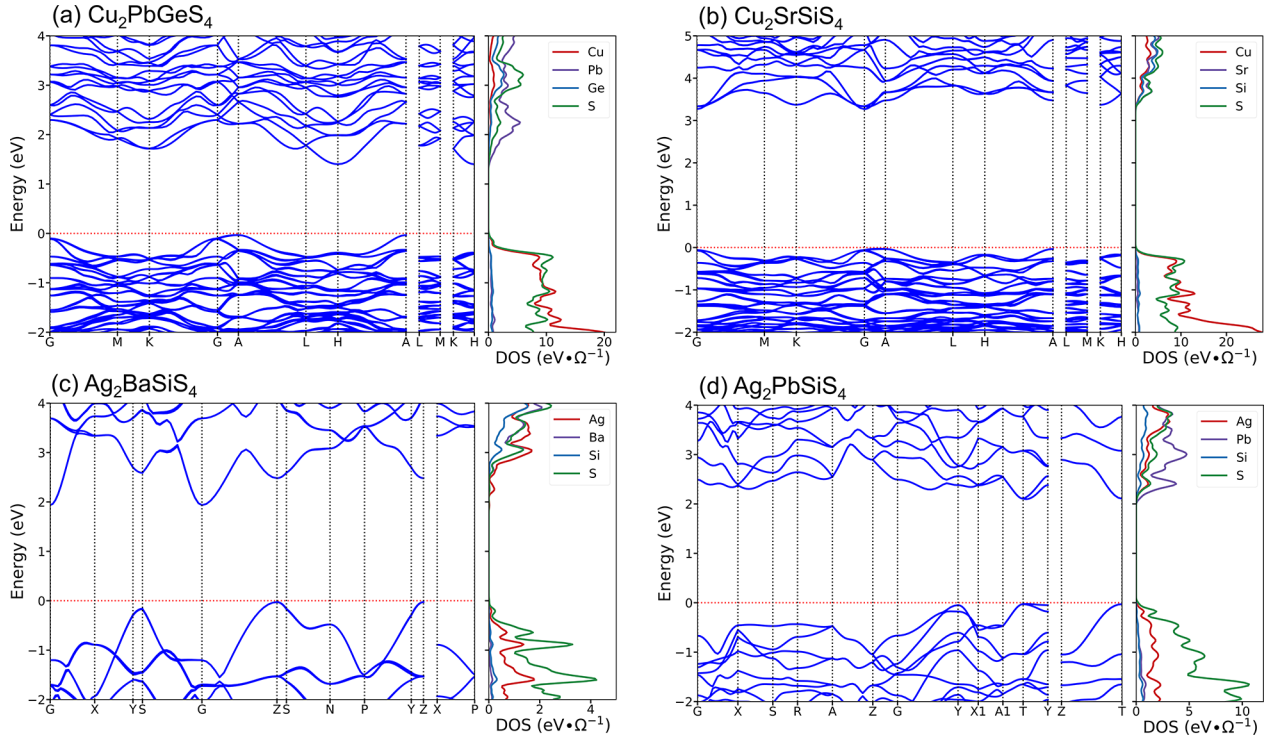

Figure 11. HSE06 calculated band structures and partial densities of states (DOS). Ω is the volume of the unit cell used in the calculation. Brillouin zones and band structure k-space paths are illustrated in Figure S1.

values. Figure S8 plots the tolerance factors for the quaternary materials, for each phase and functional. Interestingly, the tolerance factors from DFT-relaxed structures (t_I^{DFT}, t_{IV}^{DFT}) tend to cluster near the tolerance factors derived from average experimental bond lengths (t_I^{avg}, t_{IV}^{avg}), regardless of the functional used in the calculation, when the experimentally realized phase is considered. In the calculation of (t_I^{DFT}, t_{IV}^{DFT}), equations 4-5 have been modified to substitute $r_M + r_X$ with the average bond length of each DFT-relaxed structure. As an example of the above point, for Ag_2BaSiS_4, the (t_I^{DFT}, t_{IV}^{DFT}) values are closer to (t_I^{avg}, t_{IV}^{avg}) for $I\bar{4}2m$ than for $P3_1$ or $Ama2$† with no apparent advantage for any functional. Thus, computing (t_I^{DFT}, t_{IV}^{DFT}) could be considered an alternative method to using average experimental bond lengths.

Electronic Structure. To probe the electronic properties of the four quaternary materials that formed during solid state syntheses, each compound was internally relaxed with the PXRD-determined structures and lattice constants, using HSE06 with fixed values $\alpha = 0.25$ and $\omega = 0.11$ bohr^{-1} for the exchange-mixing and range-separation parameters, respectively.[57,58,93] Band structures and partial densities of states (DOS) are shown in Figure 11, with calculated bandgaps listed in Table 4. Spin−orbit coupling (SOC) was included in all calculated band structures and densities of states using a second-variational, non-selfconsistent approach.[45] Using these settings, past experience for I_2-II-IV-X_4 materials suggests that calculated bandgaps typically underestimate the experimental bandgap by ∼0.3 eV.[31] However, this particular implementation of SOC has been shown to result in uncertainty of several tenths of eV when very heavy elements are involved (note that the strength of relativistic effects increases drastically with atomic number).[45] For instance, in Ag−Bi based double perovskites investigated in past work by some of us, the associated shift amounts to ∼0.4 eV to wider bandgap of nominally unoccupied $6p_{1/2}$ orbitals of Bi, adjacent to Pb in the periodic table (see detailed discussion in the Supporting Information of ref 59). Thus, we expect the calculated bandgaps to underestimate the experimental bandgaps of Ag_2BaSiS_4 and Cu_2SrSiS_4, while potentially providing a closer estimate of the bandgaps of Ag_2PbSiS_4 and Cu_2PbGeS_4 due to some error cancellation between the hybrid functional used and SOC effects. In all four materials, the valence band maxima (VBM) are primarily composed of Ag/Cu and S states. The conduction band minima (CBM) show significantly more variation in constituent states. Ag_2BaSiS_4 has a much larger contribution from Ag, while Pb states make up the majority of the CBM in both Ag_2PbSiS_4 and Cu_2PbGeS_4; Cu_2SrSiS_4 has a more even distribution from all constituent atoms. The band structures and atomic contributions to the DOS for Ag_2BaSiS_4 and Cu_2SrSiS_4 also closely match previous calculations of related materials (e.g., Ag_2BaGeS_4, Ag_2BaSnS_4, Cu_2SrGeS_4, Cu_2SrSnS_4).[31] Calculated absorption coefficients of the four materials are shown in Figure 12. Cu_2PbGeS_4 shows the strongest optical response in the visible spectrum, although the predicted indirect nature of its bandgap is not ideal for potential application in PV devices. Ag_2PbSiS_4, with a direct bandgap at ∼2 eV, shows similar magnitude of absorption coefficients to the PV material Cu_2BaSnS_4, which also has a similar bandgap.[31] Note that, although larger than optimal for single junction PV, the ∼2 eV bandgap value for Ag_2PbSiS_4 may prove useful for tandem junction solar cells.[94]

Optical Properties. Diffuse reflectance spectra of the powder samples are plotted in Figure 13, with bandgaps listed in Table 4. Ag_2BaSiS_4 is predicted to have an indirect bandgap of 1.96 eV. The pale yellow sample color is consistent with an indirect bandgap measured at 2.2 eV, and is also in line with the expected underestimation of the bandgap from HSE06 (∼0.3 eV). Because there is a significant Ag_8SiS_6 impurity in the Ag_2PbSiS_4 sample, diffuse reflectance spectra of a reference sample of the impurity is included to justify the designation of

https://dx.doi.org/10.1021/acs.chemmater.9b05107
Chem. Mater. 2020, 32, 1636−1649

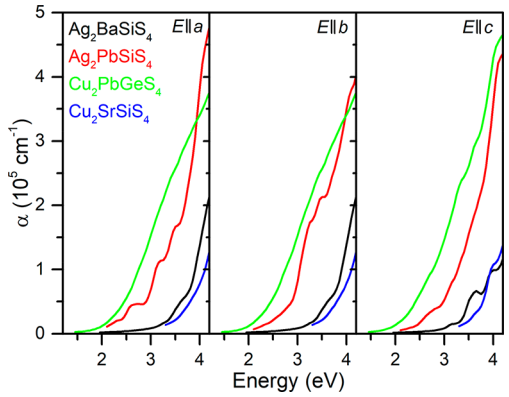

Figure 12. HSE06 calculated absorption coefficients (α) as a function of energy with the electric field (E) parallel to each reciprocal axis. A Lorentz broadening function with a full-width at half-maximum of 0.1 eV has been used to produce smooth curves. The broadening function leads to small tails below the calculated bandgaps, which are not shown because they do not reflect physical absorption processes.

the below-gap background. The direct bandgap of 1.96 eV for this material is consistent with the deep-red color and closely matches the prediction. Ag_2PbGeS_4, the other known *Ama*2† compound, shows an onset at 1.82 eV when fit as a direct bandgap material.[32] The trend of increasing bandgap when changing the IV atom from Sn to Ge to Si is expected for this class of materials and arises from Sn/Ge/Si contributions to the CBM.[31] Cu_2PbGeS_4 has an indirect bandgap of 1.55 eV, whereas the corresponding Si-analog, Cu_2PbSiS_4, has an indirect bandgap of 1.65 eV,[32] again consistent with the expected trends when replacing the IV atom. The indirect bandgap of 3.4 eV for Cu_2SrSiS_4 closely matches the predicted value (3.3 eV), despite expectations that the experimental bandgap might be slightly larger. It is not immediately obvious why the correspondence between HSE06 prediction and experimental observation should be so close in this case. However, the large uncertainty (0.3 eV) in this measurement due to the lack of a well-defined absorption edge may be afactor that affects the overall band gap determination for Cu_2SrSiS_4. With such a wide bandgap, the grayish-yellow color of this material is attributed to the small amount of impurity phases. In the $[h\nu F(R)]^{1/2}$ spectra (gray symbols) there is a weak apparent onset at ~2.1 eV that is the likely source of this color discrepancy. This absorption onset is consistent with the $Cu_{2-x}S$ impurity identified in PXRD spectra (Figure 8).[95]

CONCLUSION

From an analysis of 31 prospectively defect-resistant I_2-II-IV-X_4 compounds across five crystal structures, a set of tolerance factors has been derived that serve as descriptors of the regions in which distinct quaternary phases may occur within this chalcogenide-based materials family. Applying these tolerance factors to new I_2-II-IV-X_4 compounds is expected to aid in determining which of the five structures are likely to form. Unlike oxide and halide perovskite materials where the sum of ionic radii has often been assumed to adequately represent bond lengths, we find significant discrepancies between experimental bond lengths and those expected from ionic radii. When average experimental I_2-II-IV-X_4 family bond lengths are used (a set of values that will become even more reliable as the number of discovered/characterized I_2-II-IV-X_4 family members increases), this set of tolerance factors can be applied as a tool for materials discovery. To demonstrate the utility of this approach, four new I_2-II-IV-X_4 compounds, Ag_2BaSiS_4, Ag_2PbSiS_4, Cu_2PbGeS_4, and Cu_2SrSiS_4, have been synthesized in the predicted structure types. In conjunction with HSE06

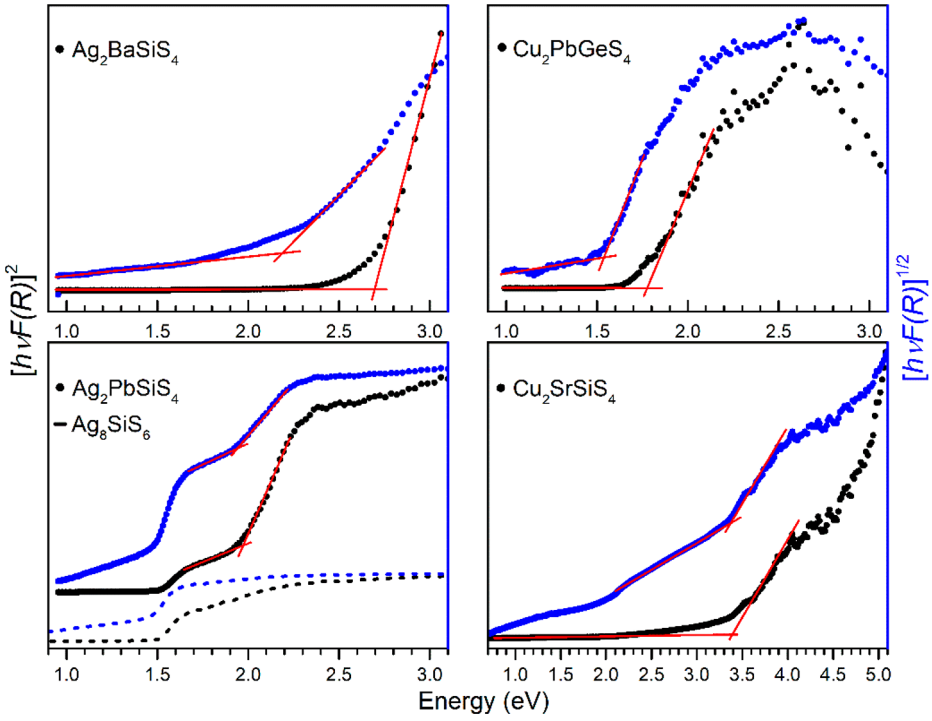

Figure 13. Diffuse reflectance spectra of Ag_2BaSiS_4, Ag_2PbSiS_4 (and Ag_8SiS_6), Cu_2PbGeS_4, and Cu_2SrSiS_4 plotted as $[h\nu F(R)]^2$ (black symbols, direct bandgap) and $[h\nu F(R)]^{1/2}$ (blue symbols, indirect bandgap), where $F(R)$ is the Kubelka–Munk function. Red lines show the fit used to extract the bandgap(s).

https://dx.doi.org/10.1021/acs.chemmater.9b05107
Chem. Mater. 2020, 32, 1636−1649

calculations, we report the experimental bandgaps and calculated band structures and optoelectronic properties for these new compounds.

■ ASSOCIATED CONTENT

Supporting Information

The Supporting Information is available free of charge at https://pubs.acs.org/doi/10.1021/acs.chemmater.9b05107.

k-Point grids and lattice parameters of calculated structures; Brillouin zones and k-paths of calculated band structures; comparison of *Ama*2 and *Ama*2† crystal structures; tolerance factor derivation; ratio of experimental bond lengths to those predicted by Shannon ionic and crystal radii; tolerance factor plot of average experimental bond lengths with all compounds labeled; simulated PXRD pattern of Ag_2PbSiS_4 with preferred orientation; DFT formation energies with SCAN results (PDF)

■ AUTHOR INFORMATION

Corresponding Author

David B. Mitzi − *Department of Mechanical Engineering and Materials Science and Department of Chemistry, Duke University, Durham, North Carolina 27708, United States;* orcid.org/0000-0001-5189-4612; Email: david.mitzi@duke.edu

Authors

Jon-Paul Sun − *Department of Mechanical Engineering and Materials Science, Duke University, Durham, North Carolina 27708, United States*

Garrett C. McKeown Wessler − *Department of Mechanical Engineering and Materials Science, Duke University, Durham, North Carolina 27708, United States*

Tianlin Wang − *Department of Mechanical Engineering and Materials Science, Duke University, Durham, North Carolina 27708, United States*

Tong Zhu − *Department of Mechanical Engineering and Materials Science, Duke University, Durham, North Carolina 27708, United States*

Volker Blum − *Department of Mechanical Engineering and Materials Science and Department of Chemistry, Duke University, Durham, North Carolina 27708, United States;* orcid.org/0000-0001-8660-7230

Complete contact information is available at: https://pubs.acs.org/10.1021/acs.chemmater.9b05107

Notes

The authors declare no competing financial interest.

■ ACKNOWLEDGMENTS

This material is based upon work supported by the U.S. Department of Energy, Office of Science, Basic Energy Sciences (BES), under Contract DE-SC0020061, as well as by the Duke University Energy Initiative Research Seed Fund. J.P.S. thanks the Natural Sciences and Engineering Research Council of Canada for a postdoctoral fellowship. G.C.M.W. acknowledges the support of the National Science Foundation Graduate Research Fellowship Program under Grant DGE-1644868. The authors thank Zachary Widel in the lab of Dr. Michael Therien for assistance with diffuse reflectance measurements.

■ ADDITIONAL NOTE

[a]During the review process, Cu_2SrSiS_4 was independently reported in ref 39. We have included this information in all relevant figures and tables.

■ REFERENCES

(1) Zakutayev, A. Brief Review of Emerging Photovoltaic Absorbers. *Curr. Opin. Green Sustain. Chem.* **2017**, *4*, 8−15.

(2) Shi, Y.; Sturm, C.; Kleinke, H. Chalcogenides as Thermoelectric Materials. *J. Solid State Chem.* **2019**, *270*, 273−279.

(3) Bonnick, P.; Blanc, L.; Vajargah, S. H.; Lee, C.-W.; Sun, X.; Balasubramanian, M.; Nazar, L. F. Insights into Mg^{2+} Intercalation in a Zero-Strain Material: Thiospinel $Mg_xZr_2S_4$. *Chem. Mater.* **2018**, *30*, 4683−4693.

(4) Kaup, K.; Lalère, F.; Huq, A.; Shyamsunder, A.; Adermann, T.; Hartmann, P.; Nazar, L. F. Correlation of Structure and Fast Ion Conductivity in the Solid Solution Series $Li_{1+2x}Zn_{1-x}PS_4$. *Chem. Mater.* **2018**, *30*, 592−596.

(5) Zhang, Z.; Ramos, E.; Lalere, F.; Assoud, A.; Kaup, K.; Hartman, P.; Nazar, L. F. $Na_{11}Sn_2PS_{12}$: A New Solid State Sodium Superionic Conductor. *Energy Environ. Sci.* **2018**, *11*, 87−93.

(6) Milliron, D. J.; Mitzi, D. B.; Copel, M.; Murray, C. E. Solution-Processed Metal Chalcogenide Films for p-Type Transistors. *Chem. Mater.* **2006**, *18*, 587−590.

(7) Kwon, S. M.; Won, J. K.; Jo, J.-W.; Kim, J.; Kim, H.-J.; Kwon, H.-I.; Kim, J.; Ahn, S.; Kim, Y.-H.; Lee, M.-J.; et al. High-Performance and Scalable Metal-Chalcogenide Semiconductors and Devices via Chalco-Gel Routes. *Sci. Adv.* **2018**, *4*, No. eaap9104.

(8) Eggleton, B. J.; Luther-Davies, B.; Richardson, K. Chalcogenide Photonics. *Nat. Photonics* **2011**, *5*, 141−148.

(9) Hudgens, S.; Johnson, B. Overview of Phase-Change Chalcogenide Nonvolatile Memory Technology. *MRS Bull.* **2004**, *29*, 829−832.

(10) Green, M. A.; Hishikawa, Y.; Dunlop, E. D.; Levi, D. H.; Hohl-Ebinger, J.; Yoshita, M.; Ho-Baillie, A. W. Y. Solar Cell Efficiency Tables (Version 53). *Prog. Photovoltaics* **2019**, *27*, 3−12.

(11) Feltrin, A.; Freundlich, A. Material Considerations for Terawatt Level Deployment of Photovoltaics. *Renewable Energy* **2008**, *33*, 180−185.

(12) Tao, C. S.; Jiang, J.; Tao, M. Natural Resource Limitations to Terawatt-Scale Solar Cells. *Sol. Energy Mater. Sol. Cells* **2011**, *95*, 3176−3180.

(13) Wang, W.; Winkler, M. T.; Gunawan, O.; Gokmen, T.; Todorov, T. K.; Zhu, Y.; Mitzi, D. B. Device Characteristics of CZTSSe Thin-Film Solar Cells with 12.6% Efficiency. *Adv. Energy Mater.* **2014**, *4*, 1301465.

(14) Gokmen, T.; Gunawan, O.; Todorov, T. K.; Mitzi, D. B. Band Tailing and Efficiency Limitation in Kesterite Solar Cells. *Appl. Phys. Lett.* **2013**, *103*, 103506.

(15) Rey, G.; Larramona, G.; Bourdais, S.; Choné, C.; Delatouche, B.; Jacob, A.; Dennler, G.; Siebentritt, S. On the Origin of Band-Tails in Kesterite. *Sol. Energy Mater. Sol. Cells* **2018**, *179*, 142−151.

(16) Nishiwaki, M.; Nagaya, K.; Kato, M.; Fujimoto, S.; Tampo, H.; Miyadera, T.; Chikamatsu, M.; Shibata, H.; Fujiwara, H. Tail State Formation in Solar Cell Materials: First Principles Analyses of Zincblende, Chalcopyrite, Kesterite, and Hybrid Perovskite Crystals. *Phys. Rev. Mater.* **2018**, *2*, 085404.

(17) Levcenko, S.; Just, J.; Redinger, A.; Larramona, G.; Bourdais, S.; Dennler, G.; Jacob, A.; Unold, T. Deep Defects in $Cu_2ZnSn(S,Se)_4$ Solar Cells with Varying Se Content. *Phys. Rev. Appl.* **2016**, *5*, 024004.

(18) Sarker, P.; Harrington, T.; Toher, C.; Oses, C.; Samiee, M.; Maria, J.-P.; Brenner, D. W.; Vecchio, K. S.; Curtarolo, S. High-Entropy High-Hardness Metal Carbides Discovered by Entropy Descriptors. *Nat. Commun.* **2018**, *9*, 4980.

(19) Chen, S.; Walsh, A.; Gong, X.-G.; Wei, S.-H. Classification of Lattice Defects in the Kesterite Cu_2ZnSnS_4 and $Cu_2ZnSnSe_4$ Earth-Abundant Solar Cell Absorbers. *Adv. Mater.* **2013**, *25*, 1522−1539.

(20) Shin, D.; Saparov, B.; Zhu, T.; Huhn, W. P.; Blum, V.; Mitzi, D. B. $BaCu_2Sn(S,Se)_4$: Earth-Abundant Chalcogenides for Thin-Film Photovoltaics. *Chem. Mater.* **2016**, *28*, 4771−4780.
(21) Shin, D.; Saparov, B.; Mitzi, D. B. Defect Engineering in Multinary Earth-Abundant Chalcogenide Photovoltaic Materials. *Adv. Energy Mater.* **2017**, *7*, 1602366.
(22) Hong, F.; Lin, W.; Meng, W.; Yan, Y. Trigonal Cu_2-II-Sn-VI_4 (II = Ba, Sr and VI = S, Se) Quaternary Compounds for Earth-Abundant Photovoltaics. *Phys. Chem. Chem. Phys.* **2016**, *18*, 4828−4834.
(23) Xiao, Z.; Meng, W.; Li, J. V.; Yan, Y. Distant-Atom Mutation for Better Earth-Abundant Light Absorbers: A Case Study of $Cu_2BaSnSe_4$. *ACS Energy Lett.* **2017**, *2*, 29−35.
(24) Shannon, R. D. Revised Effective Ionic Radii and Systematic Studies of Interatomic Distances in Halides and Chalcogenides. *Acta Crystallogr., Sect. A: Cryst. Phys., Diffr., Theor. Gen. Crystallogr.* **1976**, *32*, 751−767.
(25) Shin, D.; Zhu, T.; Huang, X.; Gunawan, O.; Blum, V.; Mitzi, D. B. Earth-Abundant Chalcogenide Photovoltaic Devices with over 5% Efficiency Based on a $Cu_2BaSn(S,Se)_4$ Absorber. *Adv. Mater.* **2017**, *29*, 1606945.
(26) Shin, D.; Ngaboyamahina, E.; Zhou, Y.; Glass, J. T.; Mitzi, D. B. Synthesis and Characterization of an Earth-Abundant $Cu_2BaSn(S,Se)_4$ Chalcogenide for Photoelectrochemical Cell Application. *J. Phys. Chem. Lett.* **2016**, *7*, 4554−4561.
(27) Zhou, Y.; Shin, D.; Ngaboyamahina, E.; Han, Q.; Parker, C. B.; Mitzi, D. B.; Glass, J. T. Efficient and Stable Pt/TiO_2/CdS/$Cu_2BaSn(S,Se)_4$ Photocathode for Water Electrolysis Applications. *ACS Energy Lett.* **2018**, *3*, 177−183.
(28) Teymur, B.; Zhou, Y.; Ngaboyamahina, E.; Glass, J. T.; Mitzi, D. B. Solution-Processed Earth-Abundant $Cu_2BaSn(S,Se)_4$ Solar Absorber Using a Low-Toxicity Solvent. *Chem. Mater.* **2018**, *30*, 6116−6123.
(29) Kuo, J. J.; Aydemir, U.; Pöhls, J.-H.; Zhou, F.; Yu, G.; Faghaninia, A.; Ricci, F.; White, M. A.; Rignanese, G.-M.; Hautier, G.; et al. Origins of Ultralow Thermal Conductivity in 1-2-1-4 Quaternary Selenides. *J. Mater. Chem. A* **2019**, *7*, 2589−2596.
(30) Li, Y.; Li, Z.; Zhang, C.; Yang, D.; Liu, T.; Yan, Y.; Liu, W.; Tan, G.; Su, X.; Uher, C.; et al. Ultralow Thermal Conductivity of $BaAg_2SnSe_4$ and the Effect of Doping by Ga and In. *Mater. Today Phys.* **2019**, *9*, 100098.
(31) Zhu, T.; Huhn, W. P.; Wessler, G. C.; Shin, D.; Saparov, B.; Mitzi, D. B.; Blum, V. I_2-II-IV-VI_4 (I = Cu, Ag; II = Sr, Ba; IV = Ge, Sn; VI = S, Se): Chalcogenides for Thin-Film Photovoltaics. *Chem. Mater.* **2017**, *29*, 7868−7879.
(32) Nhalil, H.; Han, D.; Du, M.-H.; Chen, S.; Antonio, D.; Gofryk, K.; Saparov, B. Optoelectronic Properties of Candidate Photovoltaic Cu_2PbSiS_4, Ag_2PbGeS_4 and KAg_2SbS_4 Semiconductors. *J. Alloys Compd.* **2018**, *746*, 405−412.
(33) Tong, Z.; Yuan, J.; Chen, J.; Wu, A.; Huang, W.; Han, C.; Cai, Q.; Ma, C.; Liu, Y.; Fang, L.; et al. Optical and Photoelectrochemical Properties of Cu_2SrSnS_4 Thin Film Fabricated by a Facial Ball-Milling Method. *Mater. Lett.* **2019**, *237*, 130−133.
(34) Azam, S.; Irfan, M.; Abbas, Z.; Khan, S. A.; Kityk, I. V.; Kanwal, T.; Sohail, M.; Muhammad, S.; Al-Sehemi, A. G. Effect of S and Se Replacement on Electronic and Thermoelectric Features of $BaCu_2GeQ_4$ (Q = S, Se) Chalcogenide Crystals. *J. Alloys Compd.* **2019**, *790*, 666−674.
(35) Nian, L.; Huang, J.; Wu, K.; Su, Z.; Yang, Z.; Pan, S. $BaCu_2M^{IV}Q_4$ (M^{IV} = Si, Ge, and Sn; Q = S, Se): Synthesis, Crystal Structures, Optical Performances and Theoretical Calculations. *RSC Adv.* **2017**, *7*, 29378−29385.
(36) Nian, L.; Wu, K.; He, G.; Yang, Z.; Pan, S. Effect of Element Substitution on Structural Transformation and Optical Performances in $I_2BaM^{IV}Q_4$ (*I* = Li, Na, Cu, and Ag; M^{IV} = Si, Ge, and Sn; Q = S and Se). *Inorg. Chem.* **2018**, *57*, 3434−3442.
(37) Wessler, G. C.; Zhu, T.; Sun, J.-P.; Harrell, A.; Huhn, W. P.; Blum, V.; Mitzi, D. B. Band Gap Tailoring and Structure-Composition Relationship within the Alloyed Semiconductor $Cu_2BaGe_{1-x}Sn_xSe_4$. *Chem. Mater.* **2018**, *30*, 6566−6574.
(38) Goldschmidt, V. M. Die Gesetze der Krystallochemie. *Naturwissenschaften* **1926**, *14*, 477−485.
(39) Yang, Y.; Wu, K.; Zhang, B.; Gao, L. New family of quaternary thiosilicates SrA_2SiS_4 (A = Li, Na, Cu) as promising infrared nonlinear optical crystals. *J. Mater. Chem. C* **2019**, Accepted manuscript DOI: 10.1039/C9TC06077D.
(40) Kubelka, P.; Munk, F. Ein Beitrag Zur Optik Der Farbanstriche. *Z. Für Technol. Phys.* **1931**, *12*, 593−601.
(41) Blum, V.; Gehrke, R.; Hanke, F.; Havu, P.; Havu, V.; Ren, X.; Reuter, K.; Scheffler, M. Ab Initio Molecular Simulations with Numeric Atom-Centered Orbitals. *Comput. Phys. Commun.* **2009**, *180*, 2175−2196.
(42) Ren, X.; Rinke, P.; Blum, V.; Wieferink, J.; Tkatchenko, A.; Sanfilippo, A.; Reuter, K.; Scheffler, M. Resolution-of-Identity Approach to Hartree-Fock, Hybrid Density Functionals, RPA, MP2 and *GW* with Numeric Atom-Centered Orbital Basis Functions. *New J. Phys.* **2012**, *14*, 053020.
(43) Havu, V.; Blum, V.; Havu, P.; Scheffler, M. Efficient Integration for All-Electron Electronic Structure Calculation Using Numeric Basis Functions. *J. Comput. Phys.* **2009**, *228*, 8367−8379.
(44) Knuth, F.; Carbogno, C.; Atalla, V.; Blum, V.; Scheffler, M. All-Electron Formalism for Total Energy Strain Derivatives and Stress Tensor Components for Numeric Atom-Centered Orbitals. *Comput. Phys. Commun.* **2015**, *190*, 33−50.
(45) Huhn, W. P.; Blum, V. One-Hundred-Three Compound Band-Structure Benchmark of Post-Self-Consistent Spin-Orbit Coupling Treatments in Density Functional Theory. *Phys. Rev. Mater.* **2017**, *1*, 033803.
(46) Jensen, S. R.; Saha, S.; Flores-Livas, J. A.; Huhn, W.; Blum, V.; Goedecker, S.; Frediani, L. The Elephant in the Room of Density Functional Theory Calculations. *J. Phys. Chem. Lett.* **2017**, *8*, 1449−1457.
(47) Lejaeghere, K.; Bihlmayer, G.; Bjorkman, T.; Blaha, P.; Blugel, S.; Blum, V.; Caliste, D.; Castelli, I. E.; Clark, S. J.; Dal Corso, A.; et al. Reproducibility in Density Functional Theory Calculations of Solids. *Science* **2016**, *351*, No. aad3000.
(48) Levchenko, S. V.; Ren, X.; Wieferink, J.; Johanni, R.; Rinke, P.; Blum, V.; Scheffler, M. Hybrid Functionals for Large Periodic Systems in an All-Electron, Numeric Atom-Centered Basis Framework. *Comput. Phys. Commun.* **2015**, *192*, 60−69.
(49) Ihrig, A. C.; Wieferink, J.; Zhang, I. Y.; Ropo, M.; Ren, X.; Rinke, P.; Scheffler, M.; Blum, V. Accurate Localized Resolution of Identity Approach for Linear-Scaling Hybrid Density Functionals and for Many-Body Perturbation Theory. *New J. Phys.* **2015**, *17*, 093020.
(50) Perdew, J. P.; Burke, K.; Ernzerhof, M. Generalized Gradient Approximation Made Simple. *Phys. Rev. Lett.* **1996**, *77*, 3865−3868.
(51) Perdew, J. P.; Ruzsinszky, A.; Csonka, G. I.; Vydrov, O. A.; Scuseria, G. E.; Constantin, L. A.; Zhou, X.; Burke, K. Restoring the Density-Gradient Expansion for Exchange in Solids and Surfaces. *Phys. Rev. Lett.* **2008**, *100*, 136406.
(52) Sun, J.; Ruzsinszky, A.; Perdew, J. P. Strongly Constrained and Appropriately Normed Semilocal Density Functional. *Phys. Rev. Lett.* **2015**, *115*, 036402.
(53) Zhang, Y.; Kitchaev, D. A.; Yang, J.; Chen, T.; Dacek, S. T.; Sarmiento-Pérez, R. A.; Marques, M. A. L.; Peng, H.; Ceder, G.; Perdew, J. P.; et al. Efficient First-Principles Prediction of Solid Stability: Towards Chemical Accuracy. *Npj Comput. Mater.* **2018**, *4*, 9.
(54) Bartók, A. P.; Yates, J. R. Regularized SCAN Functional. *J. Chem. Phys.* **2019**, *150*, 161101.
(55) Furness, J. W.; Sun, J. Enhancing the efficiency of density functionals with an improved iso-orbital indicator. *Phys. Rev. B: Condens. Matter Mater. Phys.* **2019**, *99*, 041119.
(56) Zhang, I. Y.; Ren, X.; Rinke, P.; Blum, V.; Scheffler, M. Numeric Atom-Centered-Orbital Basis Sets with Valence-Correlation Consistency from H to Ar. *New J. Phys.* **2013**, *15*, 123033.
(57) Heyd, J.; Scuseria, G. E.; Ernzerhof, M. Hybrid Functionals Based on a Screened Coulomb Potential. *J. Chem. Phys.* **2003**, *118*, 8207−8215.

(58) Heyd, J.; Scuseria, G. E.; Ernzerhof, M. Erratum: "Hybrid Functionals Based on a Screened Coulomb Potential" [J. Chem. Phys. 118, 8207 (2003)]. *J. Chem. Phys.* **2006**, *124* (21), 219906.
(59) Jana, M. K.; Janke, S. M.; Dirkes, D. J.; Dovletgeldi, S.; Liu, C.; Qin, X.; Gundogdu, K.; You, W.; Blum, V.; Mitzi, D. B. Direct-Bandgap 2D Silver-Bismuth Iodide Double Perovskite: The Structure-Directing Influence of an Oligothiophene Spacer Cation. *J. Am. Chem. Soc.* **2019**, *141*, 7955−7964.
(60) Teske, C. L. Darstellung Und Kristallstruktur von Silber-Barium-Thiogermanat(IV). Ag_2BaGeS_4/Preparation and Crystal Structure of Silver-Barium-Thiogermanate(IV). Ag_2BaGeS_4. *Z. Naturforsch., B: J. Chem. Sci.* **1979**, *34*, 544−547.
(61) Tampier, M.; Johrendt, D. Kristallstrukturen und chemische Bindung von AM_2GeSe_4 (A = Sr, Ba; M = Cu, Ag). *Z. Anorg. Allg. Chem.* **2001**, *627*, 312−320.
(62) Teske, C. R. L.; Vetter, O. Ergebnisse Einer Röntgenstrukturanalyse von Silber-Barium-Thiostannat(IV), Ag_2BaSnS_4. *Z. Anorg. Allg. Chem.* **1976**, *427*, 200−204.
(63) Assoud, A.; Soheilnia, N.; Kleinke, H. New Quaternary Barium Copper/Silver Selenostannates: Different Coordination Spheres, Metal-Metal Interactions, and Physical Properties. *Chem. Mater.* **2005**, *17*, 2255−2261.
(64) Kogut, Yu; Fedorchuk, A.; Zhbankov, O.; Romanyuk, Ya.; Kityk, I.; Piskach, L.; Parasyuk, O. Isothermal Section of the Ag_2S-PbS-GeS_2 System at 300K and the Crystal Structure of Ag_2PbGeS_4. *J. Alloys Compd.* **2011**, *509*, 4264−4267.
(65) Teske, C. L. Über Die Darstellung Und Röntgenographische Untersuchung von Cu_2SrGeS_4 Und Cu_2BaGeS_4/On the Preparation and X-Ray Investigation of Cu_2SrGeS_4 and Cu_2BaGeS_4. *Z. Naturforsch., B: J. Chem. Sci.* **1979**, *34*, 386−389.
(66) Teske, C. L.; Vetter, O. Präparative und röntgenographische Untersuchung am System $Cu_{2-x}Ag_xBaSnS_4$. *Z. Anorg. Allg. Chem.* **1976**, *426*, 281−287.
(67) Llanos, J.; Mujica, C.; Sánchez, V.; Peña, O. Physical and Optical Properties of the Quaternary Sulfides $SrCu_2MS_4$ and $EuCu_2MS_4$ (M = Ge and Sn). *J. Solid State Chem.* **2003**, *173*, 78−82.
(68) Sun, Z.-D.; Chi, Y.; Guo, S.-P. Cu_2EuMQ_4 (M = Si, Ge; Q = S, Se): Syntheses, Structure Study and Physical Properties Determination. *J. Solid State Chem.* **2019**, *269*, 225−232.
(69) Aitken, J. A.; Lekse, J. W.; Yao, J.-L.; Quinones, R. Synthesis, Structure and Physicochemical Characterization of a Noncentrosymmetric, Quaternary Thiostannate: $EuCu_2SnS_4$. *J. Solid State Chem.* **2009**, *182*, 141−146.
(70) Olekseyuk, I. D.; Piskach, L. V.; Zhbankov, O. Ye.; Parasyuk, O. V.; Kogut, Yu. M. Phase Diagrams of the Quasi-Binary Systems Cu_2S-SiS_2 and Cu_2SiS_3-PbS and the Crystal Structure of the New Quaternary Compound Cu_2PbSiS_4. *J. Alloys Compd.* **2005**, *399*, 149−154.
(71) Teske, C. L. Darstellung und Kristallstruktur von Cu_2SrSnS_4. *Z. Anorg. Allg. Chem.* **1976**, *419*, 67−76.
(72) Wu, K.; Zhang, B.; Yang, Z.; Pan, S. New Compressed Chalcopyrite-like $Li_2BaM^{IV}Q_4$ (M^{IV} = Ge, Sn; Q = S, Se): Promising Infrared Nonlinear Optical Materials. *J. Am. Chem. Soc.* **2017**, *139*, 14885−14888.
(73) Gard, J. A.; West, A. R. Preparation and Crystal Structure of Li_2CaSiO_4 and Isostructural Li_2CaGeO_4. *J. Solid State Chem.* **1973**, *7*, 422−427.
(74) Aitken, J. A.; Larson, P.; Mahanti, S. D.; Kanatzidis, M. G. Li_2PbGeS_4 and Li_2EuGeS_4: Polar Chalcopyrites with a Severe Tetragonal Compression. *Chem. Mater.* **2001**, *13*, 4714−4721.
(75) Haferkorn, B.; Meyer, G. Li_2EuSiO_4, ein Europium(II)-dilithosilicat: Eu[$(Li_2Si)O_4$]. *Z. Anorg. Allg. Chem.* **1998**, *624*, 1079−1081.
(76) Shannon, R. D.; Gumerman, P. S. Effect of Covalence on Interatomic Distances in Cu^+, Ag^+, Tl^+ and Pb^{2+} Halides and Chalcogenides. *J. Inorg. Nucl. Chem.* **1976**, *38*, 699−703.
(77) Travis, W.; Glover, E. N. K.; Bronstein, H.; Scanlon, D. O.; Palgrave, R. G. On the Application of the Tolerance Factor to Inorganic and Hybrid Halide Perovskites: A Revised System. *Chem. Sci.* **2016**, *7*, 4548−4556.
(78) Allred, A. L. Electronegativity Values from Thermochemical Data. *J. Inorg. Nucl. Chem.* **1961**, *17*, 215−221.
(79) Bratsch, S. G. Revised Mulliken Electronegativities: I. Calculation and Conversion to Pauling Units. *J. Chem. Educ.* **1988**, *65*, 34.
(80) Allred, A. L.; Rochow, E. G. A Scale of Electronegativity Based on Electrostatic Force. *J. Inorg. Nucl. Chem.* **1958**, *5*, 264−268.
(81) Goldschmidt, V. M. Crystal Structure and Chemical Constitution. *Trans. Faraday Soc.* **1929**, *25*, 253.
(82) Cahen, D. Atomic Radii in Ternary Adamantines. *J. Phys. Chem. Solids* **1988**, *49*, 103−111.
(83) Ghiringhelli, L. M.; Vybiral, J.; Levchenko, S. V.; Draxl, C.; Scheffler, M. Big Data of Materials Science: Critical Role of the Descriptor. *Phys. Rev. Lett.* **2015**, *114*, 105503.
(84) Ghiringhelli, L. M.; Vybiral, J.; Ahmetcik, E.; Ouyang, R.; Levchenko, S. V.; Draxl, C.; Scheffler, M. Learning Physical Descriptors for Materials Science by Compressed Sensing. *New J. Phys.* **2017**, *19*, 023017.
(85) Goldsmith, B. R.; Boley, M.; Vreeken, J.; Scheffler, M.; Ghiringhelli, L. M. Uncovering Structure-Property Relationships of Materials by Subgroup Discovery. *New J. Phys.* **2017**, *19*, 013031.
(86) Bialon, A. F.; Hammerschmidt, T.; Drautz, R. Three-Parameter Crystal-Structure Prediction for *sp- d*-Valent Compounds. *Chem. Mater.* **2016**, *28*, 2550−2556.
(87) Oliynyk, A. O.; Antono, E.; Sparks, T. D.; Ghadbeigi, L.; Gaultois, M. W.; Meredig, B.; Mar, A. High-Throughput Machine-Learning-Driven Synthesis of Full-Heusler Compounds. *Chem. Mater.* **2016**, *28*, 7324−7331.
(88) Bellman, R. E. *Adaptive Control Processes: A Guided Tour*. Princeton University Press, Princeton, NJ, 2015.
(89) Levchenko, A. A.; Li, G.; Boerio-Goates, J.; Woodfield, B. F.; Navrotsky, A. TiO_2 Stability Landscape: Polymorphism, Surface Energy, and Bound Water Energetics. *Chem. Mater.* **2006**, *18*, 6324−6332.
(90) Grønvold, F.; Westrum, E. F. Heat Capacities of Iron Disulfides Thermodynamics of Marcasite from 5 to 700 K, Pyrite from 300 to 780 K, and the Transformation of Marcasite to Pyrite. *J. Chem. Thermodyn.* **1976**, *8*, 1039−1048.
(91) Cui, Z.-H.; Wu, F.; Jiang, H. First-Principles Study of Relative Stability of Rutile and Anatase TiO_2 Using the Random Phase Approximation. *Phys. Chem. Chem. Phys.* **2016**, *18*, 29914−29922.
(92) Zhang, M. Y.; Cui, Z. H.; Jiang, H. Relative Stability of FeS_2 Polymorphs with the Random Phase Approximation Approach. *J. Mater. Chem. A* **2018**, *6*, 6606−6616.
(93) Krukau, A. V.; Vydrov, O. A.; Izmaylov, A. F.; Scuseria, G. E. Influence of the Exchange Screening Parameter on the Performance of Screened Hybrid Functionals. *J. Chem. Phys.* **2006**, *125*, 224106.
(94) Vos, A. D. Detailed Balance Limit of the Efficiency of Tandem Solar Cells. *J. Phys. D: Appl. Phys.* **1980**, *13*, 839−846.
(95) Behboudnia, M.; Khanbabaee, B. Investigation of Nanocrystalline Copper Sulfide Cu_7S_4 Fabricated by Ultrasonic Radiation Technique. *J. Cryst. Growth* **2007**, *304*, 158−162.

https://dx.doi.org/10.1021/acs.chemmater.9b05107
Chem. Mater. 2020, 32, 1636−1649